Vanadium electronic configuration determination from L2,3 transition in V-oxide compounds and roscoelite

Pierre-Marie Zanetta, Maxwell Drexler, Isabel Barton, Thomas Zega

OXFORD UNIVERSITY PRESS | Microscopy and Microanalysis

Vanadium electronic configuration determination from L2,3 transition in V-oxide compounds and roscoelite.

Journal:	*Microscopy and Microanalysis*
Manuscript ID	Draft
Manuscript Type:	Original Article
Date Submitted by the Author:	n/a
Complete List of Authors:	Zanetta, Pierre-marie; The University of Arizona Department of Planetary Sciences and Lunar and Planetary Laboratory, Drexler, Maxwell; The University of Arizona, Mining & Geological Engineering Barton, Isabel; The University of Arizona, Mining & Geological Engineering Zega, Tom; The University of Arizona, Lunar and Planetary Laboratory; The University of Arizona, Materials Science and Engineering
Keywords:	Vanadium, V oxidation state, STEM-EELS, DFT calculations, Site occupancy
Abstract:	We report on the electronic structure of vanadium in synthetic V-oxides and in natural roscoelite (V-rich phyllosilicate). This study applied electron energy loss spectroscopy (EELS) in the scanning transmission electron microscope (STEM), combined with first-principles calculations, to 1) establish relationships between the V oxidation state and EELS L2,3 features and 2) better constrain the oxidation state and crystallographic siting of V in roscoelite, with implications for other V-bearing phyllosilicates. Both EELS measurements and band-structure calculations show that the EELS L3/L2 ratio decreases as the oxidation state of V increases. We establish a quantitative relationship between the V L2,3 near-edge structure and the V oxidation state by normalizing the L2 maximum peak intensity to the L3 peak intensity. Applying this method to roscoelite, we find that it hosts a mix of trivalent and tetravalent V distributed between the octahedral and tetrahedral sites with a $V^{4+}/\Sigma V = 0.6 \pm 0.1$. The developed relationship is applicable to measurements of V oxidation states in oxide and phyllosilicate minerals, which is useful for constraining the conditions of rock and mineral formation and has potential implications for metal extraction from phyllosilicate ores.

Vanadium electronic configuration determination from $L_{2,3}$ transition in V-oxide compounds and roscoelite

Pierre-Marie Zanetta[1], Maxwell S. Drexler[2], Isabel F. Barton[2], Thomas J. Zega[1,3]

1. Lunar and Planetary Laboratory, The University of Arizona, Tucson, AZ 85721, U.S.A.; 2. Mining & Geological Engineering, The University of Arizona, Tucson, AZ 85721, U.S.A. 3. Materials Science and Engineering, The University of Arizona, Tucson, AZ 85721, U.S.A.

ABSTRACT

Keywords: Vanadium, V oxidation state, STEM-EELS, DFT calculations, site occupancy,.

We report on the electronic structure of vanadium in synthetic V-oxides and in natural roscoelite (V-rich phyllosilicate). This study applied electron energy loss spectroscopy (EELS) in the scanning transmission electron microscope (STEM), combined with first-principles calculations, to 1) establish relationships between the V oxidation state and EELS $L_{2,3}$ features and 2) better constrain the oxidation state and crystallographic siting of V in roscoelite, with implications for other V-bearing phyllosilicates.

Both EELS measurements and band-structure calculations show that the EELS L_3/L_2 ratio decreases as the oxidation state of V increases. We establish a quantitative relationship between the V $L_{2,3}$ near-edge structure and the V oxidation state by normalizing the L_2 maximum peak intensity to the L_3 peak intensity. Applying this method to roscoelite, we find

that it hosts a mix of trivalent and tetravalent V distributed between the octahedral and tetrahedral sites with a $V^{4+}/\Sigma V = 0.6\pm0.1$. The developed relationship is applicable to measurements of V oxidation states in oxide and phyllosilicate minerals, which is useful for constraining the conditions of rock and mineral formation and has potential implications for metal extraction from phyllosilicate ores.

INTRODUCTION

The oxidation states of elements in natural samples can provide fundamental information on the chemical and physical conditions under which they formed or last equilibrated (Schreiber et al. 1978; Mysen et al. 1984; Ballhaus et al. 1990; Frost 1991; Petit et al. 2001; Frost and Mccammon 2008; Tian et al. 2016; Moretti and Neuville 2021; Roskosz et al. 2022). The intrinsic oxidation state of a material is related to the temperature, the composition, and the oxygen fugacity (fO_2) of the system at its origin. For instance, (Berry et al. 2008) use the Fe oxidation state of a komatiitic melt inclusion to investigate the relationship that can exist between the $Fe^{3+}/\Sigma Fe$ and the conditions (temperature, composition, water content and fO_2) of the silicate melt at their origins. Several elements may be used to help constrain the redox state of the system. The most commonly used are the 3d metals because they can occur naturally in various oxidation states and are reactive elements (Schreiber et al. 1978; Zega et al. 2003; Simon et al. 2007; Chi et al. 2009; Tan et al. 2011, 2012; Zanetta et al. 2022). One such 3d metal, vanadium (V), is widely distributed in earth and planetary materials. The prevailing valence states of V in nature are V^{3+}, V^{4+}, and V^{5+}; more reduced species containing V^{2+} and V metal are possible but vanishingly rare under earth conditions (Ostrooumov and Taran 2016). It is common for V oxides to contain V in mixed valence states (V_3O_5, V_4O_7, V_6O_{11}, V_6O_{13}, etc.).

V is overall lithophile, and most of the numerous (> 250) minerals that it forms are hydroxides or complex oxides, e.g., phosphates, vanadates, and silicates. The V-oxides are widely studied because of their material properties. V_2O_3, VO_2 and V_2O_5 are defined as

transition-metal oxides (TMOs) which can exhibit an abrupt change in their conductivity and transition from metallic to insulator above a critical temperature (Tc) (Lamsal 2014). They have unique physical, electronic, and magnetic properties and are of potential interest in numerous technologic applications, e.g., cathode material for batteries, temperature sensors, and photo-induction (Lamsal 2014; You Zhou and Ramanathan 2015). Vanadium sesquioxide (V_2O_3) is the only phase that naturally occurs above its critical temperature (160 K) and at room temperature is a metallic phase with a trigonal corundum structure and space group $R\bar{3}C$. Vanadium dioxide (VO_2) shows its transition very close to room temperature (340 K) but occurs as a monoclinic (space group $P2_1/c$) crystal structure. Lastly, vanadium pentoxide shows the highest transition temperature (Tc=530K) and occurs at room temperature as simple orthorhombic lattice with space group Pmmn (No. 59). In comparison, two relatively common V minerals, the oxyhydroxide montroseite (V,Fe)O(OH) and the phyllosilicate roscoelite (a V-bearing mica idealized as $K(V,Al)_2(AlSi_3)O_{10}(OH)_2$) (Brigatti et al. 2003), are commercially mined V ores.

Constraining the crystal chemistry of V in synthetic and natural materials is therefore of interest but requires techniques that can characterize the crystallographic siting of V as well as its electronic configuration (Loehman et al. 1969; Rakotoniaina et al. 1993; Lamsal 2014; Marcelli et al. 2017). There are numerous methods for determining element concentrations in minerals, but few of these methods can distinguish between different oxidation states or sites. The most common techniques sensitive to oxidation state are spectroscopic: Mossbauer spectroscopy (Mysen et al. 1984; Holtstam 1996; Jayasuriya et al. 2004; Roskosz et al. 2022), X-ray absorption near-edge structure (XANES) in the synchrotron transmission X-ray microscope

(STXM) (Petit et al. 2001; Simon et al. 2007; Le Guillou et al. 2015), and electron energy loss spectroscopy (EELS) in the transmission electron microscope (TEM) (Garvie et al. 1994; Garvie and Buseck 1998; Van Aken et al. 1998; Van Aken and Liebscher 2002; Zega et al. 2003; Tan et al. 2011, 2012; Bourdelle et al. 2013; Zanetta et al. 2022). However, V does not have an isotope suitable for oxidation state measurements by Mossbauer. Furthermore, because V mainly occurs in complex minerals with multiple sites that can accommodate 3d metals, high-resolution techniques that can resolve the site occupancy is of importance. STXM is a high spectral-resolution (0.1 eV) technique but is spatially limited to few tens of a nanometers and so while it can provide usefully information on crystal chemistry, it cannot provide atomic-scale site location of the V. In contrast, new-generation aberration-corrected TEMs can achieve atomic resolution while integrating EELS spectroscopic measurements with enough spectral resolution (<0.4 eV in cold field emission; <0.1 eV if monochromated) to obtain information on electronic structures of *3d* metals in a wide range of materials (Muller et al. 2008; Ek et al. 2017; Zanetta et al. 2022).

The electronic structures and spectroscopic signatures of 3d metals are complex due to their sensitivity to numerous parameters including bonding, electronic neighborhood, mixed oxidation state, crystal-field effects, and thermoelectric transitions like TMOs, e.g., Fischer 1970; Stoyanov et al. 2007; Lamsal 2014; Levina et al. 2014; Zanetta et al. 2022). Thus, a combined approach involving experimental (EELS) and density functional theory (DFT) is a powerful tool for determining the oxidations states of 3d metals and the underlying physics of electronic transitions, e.g., (Leapman et al. 1982; Brik et al. 2006; Hébert 2007; Virdi et al. 2013;

Lamsal 2014; Nuñez 2019; Zanetta et al. 2022). DFT calculations, in the last decade, have become more widely used in studying electronic structures and to confirm spectral features (Hébert et al. 2003; Hébert 2007; Blaha et al. 2011, 2020). This computational method can provide insight into the crystal chemistry and the effect of site occupancy on the spectra features (Zanetta et al. 2022).

Here, we examine the electronic structure of V in a series of synthetic oxide standards and in roscoelite, a representative silicate mineral that naturally occurs with a high V concentration. The oxidation state of V and its crystal chemistry in roscoelite are determined via energy-dispersive spectroscopy (EDS) and EELS in an aberration-corrected scanning transmission electron microscope. Obtained $L_{2,3}$ spectra are compared with the complementary information obtained by DFT calculations. Based on these experimental and modeled results, we report a method for the quantification of V-oxidation state in V-bearing oxides and phyllosilicates using EELS and examine V siting and oxidation state in roscoelite.

MATERIALS AND METHODS

Samples

We acquired three high-purity (>99.8%) standards with known oxidation states (V_2O_3, VO_2, and V_2O_5) from commercial suppliers (Alfa Aesar and SigmaAldrich) in powder form. Standards were crushed in an agate mortar and pestle in dry conditions and deposited onto lacey-carbon

films supported by Cu-mesh TEM grids (Zanetta et al. 2022). We measured several particles that were monodisperse and electron transparent (< 50 nm in thickness).

We also examined a roscoelite $K(V,Al,Mg)_2AlSi_3O_{10}(OH)_2$ sample from the Omega mine above Placerville, Colorado (Table S1). The roscoelite composition was quantified using a Cameca SX100 electron microprobe located in the University of Arizona's Kuiper Materials Imaging and Characterization Facility (KMICF). A 2-µm probe with an accelerating voltage of 15 kV and beam current of 20 nA was used for the analyses. Mg, Na, Si and Al intensities were acquired on a TAP crystal; Ca, Ti, K, Cr, V, P, Sr, and Cl on an LPET crystal; and Fe, Mn, Cu, and Co on an LLIF crystal. Standards for the microprobe measurements are given in the Supplementary Material.

We prepared electron-transparent cross sections of the roscoelite sample using the ThermoScientific (formerly FEI) Helios NanoLab 660 G^3 focused-ion-beam scanning-electron microscope (FIB-SEM) also located in KMICF. The general procedures of FIB sample preparation, e.g., coarse cutting, lift out, and in situ thinning have been previously described (Zega et al. 2007, 2020; Zanetta et al. 2022).

STEM

The V standards and the roscoelite sample were measured using a 200 keV aberration-corrected Hitachi HF5000 scanning TEM (S/TEM). The HF5000 is equipped with a cold field-emission gun, a third-order spherical-aberration corrector for STEM mode, bright-field (BF) and annular dark field (ADF) STEM detectors and a Gatan Quantum ER (model 965) electron energy-loss spectrometer (EELS). STEM-HAADF images were acquired using a 200 keV acceleration

voltage, a 10 µA emission current, and 3.45 eV extraction voltage, a STEM condenser aperture of 25 µm, and a 2 µs dwell time. All EELS spectra were corrected for channel-to-channel gain variation and dark current. We used a condenser aperture size of 35 µm and a probe current of 330 pA, a collection angle of β=63 mrad. We used a 2.5 mm EELS entrance aperture and a dispersion of 0.25 eV/channel. A pixel time of 0.2 s for the core loss was used and 0.001 s for the low loss.

Spectra were processed using personal Python scripts (from our previous work Zanetta et al. 2022 and available at: https://github.com/ZanettaPM/Ti-Oxidation-EELS-data-processing) constructed using Hyperspy (de la Peña et al. 2021). The energy position of the low-loss and high-loss spectra from different pixels were calibrated via zero-loss peak (ZLP) centering. The π^* peak of the C K-edge at 285 eV acquired with the same energy dispersion served as a calibration point. An inverse power law (AE^{-r}) model, where E is the energy loss and A and r are constants, was used to subtract the background. An energy window measuring 20 eV, placed between 430 eV and 450 eV (for a 0.025 eV/channel dispersion), was used to fit the background function. The plural scattering contributions due to sample thickness were removed by Fourier-ratio deconvolution.

Density Functional Theory

We used density functional theory (DFT) to simulate spectra and constrain the electronic configuration of the standards and the roscoelite. We computed the electronic band structure of the V standards and roscoelite by means of the linearized augmented plane wave (LAPW)

method, as implemented in the Wien2k package (Blaha et al. 2020), and approximations to the exchange-correlation by generalized gradient approach (GGA) functionals (Perdew et al. 1996). Electronic structure calculations were conducted starting with experimentally reported crystal structures (Table 1). Initialization parameters and self-consistent field (SCF) calculation convergence rules were set according to Hébert (2007). The energy to separate core and valence states was fixed at -6 Rydberg (Ry; 1 Ry ≈ 13.605 eV), except for the sample containing Al where a value of -8 Ry was adopted because of its atomic configuration. The matrix size RKmax ($R_{mt} * K_{max}$) was kept fixed at 7.0, where K_{max} is the plane wave cutoff and R_{mt} is the smallest atomic sphere. Convergence criteria for the SCF cycle were fixed at 0.00001 Ry and 0.5 mRy/au for the energy and the force respectively. After optimization of the structure, we proceeded to the next iteration with higher k-mesh points (sampling points in the irreducible wedge of the first Brillouin zone of the material) until the theoretical electron energy-loss near-edge spectra (TELNES) between two iterations became nearly identical (average difference of the intensity integrated over the energy range being <5%). For simulating the roscoelite, we attempted to relax three distinct crystal chemistries. One calculation is a natural roscoelite with a complex crystal chemistry that breaks the symmetry of the space group (C2/m) but accounts for the various V crystallographic siting and all possible atomic neighbors $K(V^{3+},V^{4+})_2(AlSi_3)O_{10}$, whereas two others are polytypes with the same structures but simplified compositions, Roscoelite(3+): $Ba(V^{3+})_2(Al_4)O_{10}$ and Roscoelite(1:3): $K(Mg)_2(V^{3+}{}_1V^{4+}{}_3)O_{10}$. The two latter crystal chemistries conserve space-group symmetry and simulate two distinct V site configurations, octahedral and tetrahedral respectively. We established these endmember compositions in order to satisfy 1) the electro-neutrality of the structure (without the presence of the OH

radicals), 2) the atomic neighbors as expected in the solid solution (K, Ba, Mg, Al, Si and O), and 3) the expected oxidation state of the V according to the site coordination (i,e., the V is expected to be V^{3+} on the octahedral site and mostly V^{4+} on the tetrahedral site; Brigatti et al. 2003). Although these simulations are not exact replicas of the natural samples, they correctly simulate the electronic environment of the V in roscoelite while allowing the correct relaxation of the structure.

The TELNES3 program implemented in Wien2k was used to model EELS spectra from density-of-states calculations (Jorissen 2007). The splitting energy and the branching ratio were calculated statistically. We assumed no orientation dependence, so we averaged our calculations over all possible directions of the scattering vector with respect to the crystal. Spectral broadening was always simulated with the same conditions, i.e., no linearly energy-dependent valence broadening and spectrometer broadening set at 0.8 and 2.3 eV. The former broadening value was used to investigate peak splitting for lower energy dispersions (<0.25 eV/channel) in EELS. The latter broadening value does not correspond to our experimental ZLP full-width-half-maximum (FWHM) but acts as a correction factor to obtain similar $VL_{2,3}$ peak widths as the experimental spectra. We fixed a factor of 2 on the second spectrum contribution in our broadening setup to match the experimental L_2/L_3 peak ratio. We kept the core-hole lifetime of the two edges as tabulated in the TELNES3 program.

RESULTS

We acquired EELS spectra at the V $L_{2,3}$ edge for V-oxide standards and roscoelite to examine their electronic structure, compare it to our DFT calculations (Table 1), and investigate a relationship between oxidation states and spectral features. The representation of the V-compound crystal structures is given in Figure 1. Figure 2a shows the experimental spectra normalized to the individual maxima of the first peak (V_{L3}, energy range: 514.0 to 521 eV) acquired from the V-bearing reference materials. The normalization suppresses the variations in absolute intensity and the effects of thickness or concentration. Experimental spectra (Fig. 2a) show the two L_3 and L_2 peaks at approximately 518 and 525 eV (labeled a and b, see Table 2). The oxide spectra show a clear chemical shift at the V $L_{2,3}$ edge that correlates with the valence state of the material. The energy positions of the peaks (Table S2) are in agreement with previous measurements of V $L_{2,3}$ spectra of V-oxides (Fischer 1970; Brik et al. 2006; Tan et al. 2012; Levina et al. 2014). As the V oxidation state increases, the intensities of peaks 'b' and 'c' increase in comparison to peak 'a'. Peak 'c' corresponds to the pre-edge peak of the O K edge. The roscoelite sample shows a significantly more intense O peak.

We also computed EELS spectra for the V-oxide standards and roscoelite. Figure 2b shows the simulated spectra with minimum broadening. Features that compose the L_3 and L_2 edges are visible (Fig.S1). The two edges are composed of three peaks (a, a', and a" and b, b', and b"). We hereafter discuss samples in order of increasing oxidation (V_2O_3, Roscoelite (3+), Roscoelite (1:3), VO_2, V_2O_5). Samples with the lower oxidation state (the 3+ blue and pink lines Fig. 2b) show a higher subpeak a than a' and no a". As the oxidation state increases the peak a" and b" increase in intensity. In VO_2 and Roscoelite (1:3), subpeaks a', and b' increase and reach about the same intensity as the a and b peaks. The subpeaks a" and b" increase significantly. In V_2O_5,

peaks a and b decrease compared to VO_2, whereas the intensities of peaks a" and b" keep increasing. We note that peaks c and c' display no consistent trend with increasing oxidation state because they reside on top of the O K edge and only the V $L_{2,3}$ line is modeled in our calculations.

Figure 3 compares the experimental and simulated spectra after broadening to account for experimental dispersion. After normalization to the L_3 intensity, the L_2 intensity increases with increasing oxidation state (Fig. 3a and 3b dark arrows). In our simulation, the "natural" roscoelite calculation did not converge within the computational resources due to the complexity of its structure, but all other calculations converged successfully (Fig 3a and b). The computed spectra reproduce the peaks and positions in the experimental spectra of V-oxides collected using EELS. Figure 3b shows that the L_3 and L_2 peaks of the roscoelite experimental spectrum plot at similar energies to that of the R(1:3) calculated spectrum (517.7 eV and 524.5 eV respectively) and at higher energies than R(3+) (515.8 eV and 523.0 eV respectively, Table S2). The simulated V L_2 and L_3 peak width are smaller for the roscoelite R(3+) in comparison to V_2O_3 despite having the same oxidation state.

The onset energy of the V edge in roscoelite (512.8 eV) occurs at a higher energy than tetravalent V (512.5 eV) as represented by VO_2. Therefore, use of the identified chemical shift, by itself, for the quantification of the V oxidation state in roscoelite is problematic because stoichiometry suggests V^{3+} to V^{4+} for charge balance. So, we explored an alternative approach to quantify the V oxidation state in roscoelite. Our TELNES calculations show that the increase of the b peak (L_2) is predominantly dependent on the oxidation state regardless of specific site occupancies and those effects on the ELNES (Fig. 3 dark arrows). Thus, the L_2 maximum intensity

(after normalization) depends on the V oxidation state and can be used for quantifying it. We find that the maximum intensity of the L_2 peak increases as a function of increasing oxidation state (Fig. 4). A best fit to the experimental data on the oxides gives:

$$y = 0.054 \times x + 0.768 \quad (1)$$

with $R^2 = 0.99$ (Fig 4).

The fitted line defined by eq (1) is compared to the fitted line defined by the simulated spectra (dashed blue line in Fig.4 with $y = 0.088 \times x + 0.613$ and R^2=0.86). Based on scattering of the experimental data points from the oxide standards around the fitted line, we estimate an absolute error of ~ 10% for the determination of the V oxidation state (dashed black lines, Fig. 4) by this method. The application of this method to the roscoelite sample (R in Fig. 4) yields a $V^{4+}/\Sigma V$ ratio of 0.6±0.1.

DISCUSSION

Electronic structures of V oxides

The V-oxides and roscoelite samples analyzed in this study show different structures and crystal chemistries (Table 1, Fig. 1). The neighborhood of V and its interaction with O in each of these structures generates distinct ELNES spectral features (Fig. 2, 3). The interaction between the V 3d orbital and O 2p orbital forms the $2e_g$, $1t_{2g}$ bonding and $2t_{2g}$, and $3e_g$ antibonding molecular orbital levels described in Fig. 5 (Fischer 1970; Stoyanov et al. 2007; Zanetta et al. 2022). Electronic transitions from the core level to empty states above the Fermi energy (E_f)

are responsible for EELS edges (Fig. 5). For 3d metals like V, the L_3 and L_2 peaks originate from the electronic transitions from the $2p^{3/2}$ and $2p^{1/2}$ core levels, respectively, to 3d levels (i.e., the anti-bonding orbitals $2t_{2g}$, and $3e_g$). Such combinations sometimes lead to the generation of four distinct peaks due to the splitting of the five degenerate states into the twofold $3e_g$ and the threefold $2t_{2g}$ level, as is the case in Ti $L_{2,3}$ (Stoyanov et al. 2007). However, the splitting energy (<1.5 eV) of the $3e_g$ and $2t_{2g}$ level in V is too small to be visible with the present energy resolution in the EELS spectra (0.25 eV/channel). These levels are easily visible in our simulations, e.g., peaks a and a' and b and b' in V_2O_3 spectrum, which are shown with a smaller broadening energy (Fig. 2b). The splitting energy and the intensity of the peaks depend on various factors as well as the oxidation state, including the site symmetry and the crystal field (Fischer 1970; Leapman et al. 1982; Stoyanov et al. 2007). The energy of the two orbital levels (i.e., the $3e_g$ and $2t_{2g}$) can be exchanged (one passing above the other in terms of energy, Fig. 5) depending on whether the V occupies a tetrahedral or octahedral site (Zhou 2017). However, it was shown that the $3e_g$ and the $2t_{2g}$ levels exhibit close energy states for V (Lamsal 2014). These results suggest that the configurational mixing of the $3e_g$ and $2t_{2g}$ levels and octahedral distortions cannot be measured with the used energy dispersion in this study. We conclude that with the experimental energy dispersion used in this study, the effects of the degenerate states on the spectral features (Fig. 2b) are convoluted in the broadened L_2 and L_3 peak intensities (Fig. 3) and do not impact our established relationship between the V oxidation state and EELS $L_{2,3}$ features.

Calibration curve

The results of this study also shed light on the suitability of different methods for analyzing 3d metal oxidation states from EELS spectra of silicates and oxides. The peaks that constitute the V $L_{2,3}$ edge correspond to quantized electronic transitions. Establishing an accurate description of the 3d band structure is useful to understand the connection between the oxidation state and electronic structure (Fig. 5). Among those methods, white-line ratios have been widely used in the last decades to trace the chemical shift and quantify the oxidation state and numerous studies in the literature established such a relationship for various 3d metals including Fe, Ti, Mn, Cr, V, Cu, Ce e.g.; Garvie et al. 1994; Van Aken et al. 1998; Xu and Wang 1999; Petit et al. 2001; Van Aken and Liebscher 2002; Stoyanov et al. 2007; Tan et al. 2012; Bourdelle et al. 2013; Zanetta et al. 2022). Most of these relationships are based on the chemical shift of the edge onset, i.e., they quantify how the shift in edge onset energy increases as the oxidation state increases. This shift is mainly due to the increasing of the band gap width and the electron screening efficiency that increase with the oxidation state (Egerton 1996; Stoyanov et al. 2007; Zanetta et al. 2022). The white-line (WL) approach offers an attractive means of tracking the shift in energy in oxide compounds as a function of oxidation state because the effects of the crystal field and coordination environments can be neglected. However, as we show above, the application of the white line ratio to the roscoelite sample, as developed for V-oxides (Tan et al. 2012), would result in a bulk oxidation state above V^{4+}, which is inconsistent with the expected V^{3+} to V^{4+} based on roscoelite stoichiometry. One explanation for this problem could be in situ sample damage during analysis, causing oxidation. Such damage has been observed for Fe in sheet silicates (Garvie et al. 2004). However, we did not observe any features that could suggest beam damage of the V-oxide samples after the EELS

acquisition, e.g, shape changes or amorphization. Additionally, we used a large field-of-view (50 nm x 50nm) for our measurements to reduce the electron dose and minimize any potential damage of the roscoelite. Another explanation for the lack of applicability of the WL ratio to silicates could be that the peak width, which depends on the time it takes for the ionized electron to decay to the ground state, can vary according to the electronic environment (Egerton 1996). We showed that the R(3+) simulated spectrum displays a smaller peak width than V_2O_3 despite having the same oxidation state. As the 'a' and 'b' peak widths are smaller in the roscoelite sample than the V-oxides, fewer counts were integrated within the window positioned at the onset energy (Fig. 3). We conclude that decoupling the portion of the chemical shift due to the oxidation state and the electronic environment in roscoelite is challenging, which required an alternative approach.

Other EELS methods use features of the near-edge structure, originating from the electronic configuration, for quantifying the oxidation state rather than using the WL ratio (Tan et al. 2012; Bourdelle et al. 2013; Giannini 2014; Le Guillou et al. 2015; Doyle et al. 2016; Berry et al. 2017; Zanetta et al. 2022). The combination of our experimental and first-principles descriptions of the V $L_{2,3}$ edge allows us to define another relationship between the L_2 peak intensity and the V oxidation state while decoupling the effect of the crystal chemistry. The method described here, based on the L_3-normalized intensity of the L_2 peak, uses the occupancy of levels in the V-O molecular orbitals.

In all of the V compounds measured here, the molecular orbitals are filled up to the $t_{1g}(\pi^0)$. When the $2t_{2g}$ is level is almost entirely filled with electrons (as it in the case in V_2O_3), the most

probable transition will arise from $2p^{3/2}$ (smaller energy gap, Fig. 5 dark arrows). In this case the L_3 intensity would be higher compared to the L_2 peak. In the opposite case, if the $2t_{2g}$ is empty (V_2O_5), then higher-energy transitions from the $2p^{1/2}$ (longer dark arrow) become more probable to fill the $2t_{2g}$ and $3e_g$ levels and the intensity of the L_2 increases relative to the L_3 peak (energy at which spectra are normalized). Those transition probabilities are used to establish the relationship between the L_2 peak and oxidation state (eq (1), Fig. 4). However, quantifying peak intensities with a simple integration window would lead to inaccurate results due to the chemical shift of the overall edge. To avoid the effects of the shift, we instead used the maximum energy of the peak (in the energy range of 522 to 527 eV), after normalization to the L_3 peak rather than applying an integration window. This led to the relationship shown in Fig. 4, based on the L_3/L_2 intensity ratio and which is consistent with previous works (Fischer 1970; Sparrow et al. 1984; Cressey et al. 1993; Kurmaev et al. 2005; Tan et al. 2012; Kalavathi et al. 2014).

Evolution of the L_3/L_2 intensity ratio

The L_3/L_2 intensity ratio of the 3d metals can be affected by several variables. Previous work suggested that a decrease in the L_3/L_2 branching ratio occurs as a function of the oxidation state (Fischer 1970; Leapman et al. 1982; Sparrow et al. 1984; Cressey et al. 1993; Van Aken et al. 1998; Kurmaev et al. 2005; Brik et al. 2006; Tan et al. 2012; Kalavathi et al. 2014). Sparrow et al. (1984) established that this relationship exists as the d level is filled until d=5. However, Leapman et al. 1982 compared the L_3/L_2 ratio between pure metal and oxide and found that the L_3/L_2 ratio increases as oxidation state increases.

We discuss three major difficulties that can lead to confusion about the evolution of the L_3/L_2 ratio as a function of the oxidation state. 1) The common use of integration windows to quantify oxidation states can reinforce the idea that the ratio increases with oxidation state (Van Aken et al. 1998). However, because the position of the windows captures the shift in energy of these transitions it does not give the exact evolution of the peak intensities. 2) The L_2 edge in higher oxidation states exhibits broader spectral features than L_3 because of the Coster–Kronig Auger decay process, and the use of a static integration window fails to capture this larger energy range (Fischer 1970; Leapman et al. 1982). 3) The removal of the continuum beneath the edge potentially alters the effective ratio. Models to remove this continuum have included both straight lines (Garvie et al. 1994; Zega and Buseck 2003) and step functions (Van Aken et al. 1998; Van Aken and Liebscher 2002; Stoyanov et al. 2007; Giannini 2014; Zanetta et al. 2022). Such models have generally been empirical and fit without consideration of an evolving branching ratio (Egerton 1996; Van Aken et al. 1998; Van Aken and Liebscher 2002; Stoyanov et al. 2007). Therefore, if the branching ratio is not accounted for, misleading results can arise.

We suggest that the observation of a decrease in the L_3/L_2 branching ratio as a function of the oxidation state was observed in this study because these three major difficulties do not apply to our measurements. We did not use windows for integrating the L_3/L_2 ratio and in the case of vanadium-oxide materials, the V $L_{2,3}$ edge occurs next to and sits on top of the O K-edge precluding the use of continuum removal beneath the edge. We estimate that the samples measured here are thin <30nm. Thus, multiple-scattering contributions should be minimal and the Fourier-ratio deconvolution of our data set should remove them. Further, we suggest that

the evolution of the V L_3/L_2 intensity was also reproduced by our DFT calculations (independently of the sample thickness) and can be used to quantify the oxidation state (Fischer 1970; Sparrow et al. 1984; Cressey et al. 1993; Kurmaev et al. 2005; Tan et al. 2012; Kalavathi et al. 2014).

The relatively small slope (Fig. 4 and Eq. 1) identified in the relationship between the V oxidation state and L_2 intensity is due to normalizing to the L_3 maximum intensity. The difference between the maximum of the L_2 peak intensities before normalization is generally several thousand counts depending on the integration time and is therefore not the principal factor of the uncertainties. Since everything is normalized to 1, the number of counts would not strongly affect the results of the oxidation state calculation (unless the number of counts is especially low). Instead, we quantified the uncertainties on the basis of the dispersion around the fitted curve and the fit residuals. We determine an absolute error of ±10% on the measurements of the oxidation state using this relationship.

Roscoelite V oxidation state and site occupancy

The oxidation state of V in oxide and silicate minerals is commonly used in numerous earth science and planetary applications. These range from indicators of the chemical conditions of planet formation and evolution to explanations for the inconsistent dissolution behavior of V ores in leaching (Ballhaus et al. 1990; Canil 1997; Righter et al. 2006, 2016; Prytulak et al. 2013; Nicklas et al. 2016; Zheng et al. 2019, 2022; Drexler 2022). The new method presented here offers a reliable, consistent means of measuring V oxidation state in oxides and

silicates for these purposes. Previous work on the V oxidation state in roscoelite generally assumes that it substitutes into the crystal structure primarily as V^{3+} in the octahedral layer (Fig. 1) (Foster 1959; Garrels and Larsen 1959; Meunier 1994; Radwany 2021). However, Wanty and Goldhaber (1985) developed a colorimetric method to measure the V oxidation state in phyllosilicates and compared their results with thermogravimetric analysis (TGA). Their colorimetric method reported a ratio of $V^{4+}/\Sigma V=0.15$ in the roscoelite however, the TGA gave a result of $V^{4+}/\Sigma V=0.5$. The latter value is close to our results of $V^{4+}/\Sigma V=0.6\pm0.1$. Additionally, our DFT simulations (Fig. 2b) show the increase of the b' peak and the appearance of a b" sub-peak for increasing oxidation degrees. These two peaks have the effect of widening the total peak once the broadening is considered. The fact that the a and b peaks in the experimental roscoelite spectrum are larger than those in the simulated Roscoelite (3+) spectrum support the interpretation that roscoelite contains a mixture of trivalent and tetravalent V. Taken together, these two sets of results strongly suggest that phyllosilicates host a mix of trivalent, probably octahedral, and tetravalent, probably tetrahedral V. This result indicates that the assumption that all phyllosilicate-hosted V is trivalent and octahedral is an oversimplification (Zheng et al. 2019, 2022). Such results could explain the observed variability in V dissolution behavior from phyllosilicate minerals and have implications for V ore extraction (Radwany 2021; Drexler 2022; Radwany and Barton 2022).

Direct observation by STEM-EELS of the position of the V^{3+} and V^{4+} atoms in the atomic lattice would help to confirm our results and provide insights into the crystal chemistry of V-rich phyllosilicate. However, phyllosilicates can be sensitive to the electron beam and

amorphize very quickly (Egerton et al. 2004; Garvie et al. 2004; Mignaioli et al. 2009; Egerton 2013; Ilett et al. 2020). The low vanadium content in roscoelite also requires long acquisition times for detection of its oxidation state. The use of new-generation direct-electron cameras could overcome this problem by increasing the electron detection rate at this energy (Ilett et al. 2020). The development of *compressed sensing* methods could also allow a decrease in the electron dose and provide enough spatial resolution by using reconstruction algorithms (Li et al. 2018; Stevens 2018; Taillon 2018). Additionally, use of cryo-ultramicrotomy and a cryogenic holder could aid in the minimization of beam damage (Jacquemot et al. 2019).

CONCLUSIONS

We investigated the electronic structure of V oxides and roscoelite by STEM-EELS and compared our experimental data with first principles DFT calculations. The results show that the maximum peak intensity of the L_2 edge increases in comparison to the L_3 edge with an increase in oxidation state. The L_2 edge intensity, normalized to the L_3 edge intensity, is a reliable proxy for V oxidation state in both oxides and roscoelite, a phyllosilicate V ore. Our data suggest that roscoelite hosts a mix of trivalent and tetravalent V with a ratio of $V^{4+}/\Sigma V=0.6\pm0.1$. Direct atomic-scale measurement of V and its oxidation state in the roscoelite structure would be fundamental to decipher its site occupancy and to develop new methods for its extraction, but susceptibility to beam damage needs to be considered. An approach combining measurements and modelling of the kind we report here could allow for a better understanding of the 3d metal recovery efficiency in phyllosilicates ores.

446

447 **ACKNOWLEDGEMENTS**

448 Research supported by the NASA Emerging Worlds (80NSSC19K0509) and Laboratory
449 Analysis of Returned Samples (80NSSC18K1475) Programs. The DFT results are based upon High
450 Performance Computing (HPC) resources supported by the University of Arizona TRIF, UITS, and
451 Research, Innovation, and Impact (RII) and maintained by the UArizona Research Technologies
452 department. We gratefully acknowledge NASA (grants #NNX12AL47G and #NNX15AJ22G) and
453 NSF (grant #1531243) for funding of the instrumentation in the Kuiper Materials Imaging and
454 Characterization Facility at the Lunar and Planetary Laboratory, University of Arizona. Collection
455 and characterization of the roscoelite sample was a part of work also supported by the NSF
456 (grant #2045277). We thank members of the Planetary Materials Research Group at LPL for
457 helpful discussions. P-M. Z. thanks Laurinne Valentine Blanche for her help with EELS
458 spectrometer investigation.

459

460

REFERENCES CITED

Ballhaus, C., Berry, R.F., and Green, D.H. (1990) Oxygen fugacity controls in the Earth's upper mantle. Nature 1990 348:6300, 348, 437–440.

Berry, A.J., Danyushevsky, L. V, St, H., O'neill, C., Newville, M., and Sutton, S.R. (2008) Oxidation state of iron in komatiitic melt inclusions indicates hot Archaean mantle, 455.

Berry, A.J., Schofield, P.F., Kravtsova, A.N., Miller, L.A., Stephen, N.R., Walker, A.M., Soldatov, A. V., Ireland, T.R., Geraki, K., and Mosselmans, J.F.W. (2017) The limitations of hibonite as a single-mineral oxybarometer for early solar system processes. Chemical Geology, 466, 32–40.

Blaha, P., Schwarz, K., Madsen, G., Kvasnicka, D., and Luitz, J. (2011) WIEN2k, 1–223 p. User's guide, Wien2k_11.1 Vol. 1.

Blaha, P., Schwarz, K., Tran, F., Laskowski, R., Madsen, G.K.H., and Marks, L.D. (2020) WIEN2k: An APW+lo program for calculating the properties of solids. Journal of Chemical Physics, 152, 074101.

Bourdelle, F., Benzerara, K., Beyssac, O., Cosmidis, J., Neuville, D.R., Brown, G.E., and Paineau, E. (2013) Quantification of the ferric/ferrous iron ratio in silicates by scanning transmission X-ray microscopy at the Fe L2,3 edges. Contributions to Mineralogy and Petrology, 166, 423–434.

Brigatti, M.F., Caprilli, E., Marchesini, M., and Poppi, L. (2003) THE CRYSTAL STRUCTURE OF ROSCOELITE-1M. Clays and Clay Minerals, 51, 301–308.

Brik, M.G., Ogasawara, K., Ikeno, H., and Tanaka, I. (2006) THE EUROPEAN PHYSICAL JOURNAL B Fully relativistic calculations of the L 2,3-edge XANES spectra for vanadium oxides. Eur.

Phys. J. B, 51, 345–355.

Canil, D. (1997) Vanadium partitioning and the oxidation state of Archaean komatiite magmas The MgO content of komatiite lavas is an important measure of their formation temperature deep in the Archaean mantle, and forms the basis for models of the early Earth's thermal and chemical evolution.

Chi, M., Ishii, H.A., Simon, S.B., Bradley, J.P., Dai, Z., Joswiak, D., Browning, N.D., and Matrajt, G. (2009) The origin of refractory minerals in comet 81P/Wild 2. Geochimica et Cosmochimica Acta, 73, 7150–7161.

Cressey, G., Henderson, C.M.B., and van der Laan, G. (1993) Use of L-edge X-ray absorption spectroscopy to characterize multiple valence states of 3 d transition metals; a new probe for mineralogical and geochemical research. Physics and Chemistry of Minerals, 20, 111–119.

de la Peña, F., Prestat, E., Fauske, V.T., Burdet, P., Furnival, T., Jokubauskas, P., Nord, M., Ostasevicius, T., Lähnemann, J., MacArthur, K.E., and others (2021) hyperspy/hyperspy: Release v1.6.3.

Doyle, P.M., Berry, A.J., Schofield, P.F., and Mosselmans, J.F.W. (2016) The effect of site geometry, Ti content and Ti oxidation state on the Ti K-edge XANES spectrum of synthetic hibonite. Geochimica et Cosmochimica Acta, 187, 294–310.

Drexler, M.S. (2022) VANADIUM IN PHYLLOSILICATES.

Egerton, R.F. (1996) Electron Energy-Loss Spectroscopy in the Electron Microscope, 3rd editio. (Springer, Ed.)Electron Energy-Loss Spectroscopy in the Electron Microscope.

——— (2013) Control of radiation damage in the TEM. Ultramicroscopy, 127, 100–108.

505 Egerton, R.F., Li, P., and Malac, M. (2004) Radiation damage in the TEM and SEM. Micron, 35,
506 399–409.
507 Ek, M., Ramasse, Q.M., Arnarson, L., Georg Moses, P., and Helveg, S. (2017) Visualizing atomic-
508 scale redox dynamics in vanadium oxide-based catalysts. Nature Communications, 8, 305.
509 Fischer, D.W. (1970) Molecular-Orbital Interpretation of the Soft X-Ray L II,III Emission and
510 Absorption Spectra from Some Titanium and Vanadium Compounds ARTICLES YOU MAY
511 BE INTERESTED IN Band Structure and the Titanium L II, III X-Ray Emission and Absorption
512 Spectra from Pure. Journal of Applied Physics, 41, 3561.
513 Foster, M.D. (1959) Chemical study of the mineralized clays. In and E.S.L. Garrels, Robert
514 Minard, Ed., Geochemistry and mineralogy of the Colorado Plateau uranium ores pp. 121–
515 132. U.S. Geological Survey Professional Paper.
516 Frost, B.R. (1991) Chapter 1.INTRODUCTION TO OXYGEN FUGACITY AND ITS PETROLOGIC
517 IMPORTANCE. Oxide Minerals, 1–10.
518 Frost, D.J., and Mccammon, C.A. (2008) The Redox State of Earth's Mantle.
519 Garrels, R., and Larsen, E.S. (1959) Geochemistry and mineralogy of the Colorado Plateau
520 uranium ores (Geological Survey professional paper 320). Professional Paper.
521 Garvie, L.A.J., and Buseck, P.R. (1998) Ratios of ferrous to ferric iron from nanometre-sized
522 areas in minerals. Nature, 396, 667–670.
523 Garvie, L.A.J., Craven, A.J., and Brydson, R. (1994) Use of electron-energy loss near-edge fine
524 structure in the study of minerals. American Mineralogist, 79, 411–425.
525 Garvie, L.A.J., Zega, T.J., Rez, P., and Buseck, P.R. (2004) Nanometer-scale measurements of
526 Fe3+/ΣFe by electron energy-loss spectroscopy: A cautionary note. American Mineralogist,

89, 1610–1616.

Giannini, M. (2014) The crystal chemistry of hibonite: an indicator for oxygen fugacity during Solar nebula condensation? Thesis.

Hébert, C. (2007, January 1) Practical aspects of running the WIEN2k code for electron spectroscopy. Micron. Elsevier Ltd.

Hébert, C., Luitz, J., and Schattschneider, P. (2003) Improvement of energy loss near edge structure calculation using Wien2k. In Micron Vol. 34, pp. 219–225. Elsevier Ltd.

Holtstam, D. (1996) Iron in hibonite: A spectroscopic study. Physics and Chemistry of Minerals, 23, 452–460.

Ilett, M., S'ari, M., Freeman, H., Aslam, Z., Koniuch, N., Afzali, M., Cattle, J., Hooley, R., Roncal-Herrero, T., Collins, S.M., and others (2020) Analysis of complex, beam-sensitive materials by transmission electron microscopy and associated techniques. Philosophical Transactions of the Royal Society A: Mathematical, Physical and Engineering Sciences, 378, 20190601.

Jacquemot, P., Viennet, J.C., Bernard, S., Le Guillou, C., Rigaud, B., Delbes, L., Georgelin, T., and Jaber, M. (2019) The degradation of organic compounds impacts the crystallization of clay minerals and vice versa. Scientific Reports, 9, 20251.

Jayasuriya, K.D., O'Neill, H.S.C., Berry, A.J., and Campbell, S.J. (2004) A Mössbauer study of the oxidation state of Fe in silicate melts. American Mineralogist, 89, 1597–1609.

Jorissen, K. (2007) The ab initio calculation of relativistic electron energy loss spectra. Ph. D. thesis.

Kalavathi, S., Amirthapandian, S., Chandra, S., Sahu, P.C., and Sahu, H.K. (2014) Valence state,

549 hybridization and electronic band structure in the charge ordered AlV2O4. Journal of
550 Physics Condensed Matter, 26.
551 Kurmaev, E.Z., Ankudinov, A.L., Rehr, J.J., Finkelstein, L.D., Karimov, P.F., and Moewes, A. (2005)
552 The L2:L3 intensity ratio in soft X-ray emission spectra of 3d-metals. Journal of Electron
553 Spectroscopy and Related Phenomena, 148, 1–4.
554 Lamsal, C. (2014) Electronic , thermoelectric and optical properties of vanadium oxides : VO2 ,
555 V2O3 and V2O5 Copyright Warning & Restrictions.
556 Le Guillou, C., Changela G., H., Brearley, A.J., Changela, H.G., and Brearley, A.J. (2015)
557 Widespread oxidized and hydrated amorphous silicates in CR chondrites matrices:
558 Implications for alteration conditions and H2 degassing of asteroids. Earth and Planetary
559 Science Letters, 420, 162–173.
560 Leapman, R.D., Grunes, L.A., and Fejes, P.L. (1982) Study of the L23 edges in the 3d transition
561 metals and their oxides by electron-energy-loss spectroscopy with comparisons to theory.
562 Physical Review B, 26, 614–635.
563 Levina, Aviva, Mcleod, Andrew I, Lay, Peter A, Levina, A, Mcleod, A I, and Lay, P A (2014)
564 Vanadium Speciation by XANES Spectroscopy: A Three-Dimensional Approach**. Chem.
565 Eur. J, 20, 12056–12060.
566 Li, X., Dyck, O., Kalinin, S. V, and Jesse, S. (2018) Compressed Sensing of Scanning Transmission
567 Electron Microscopy (STEM) With Nonrectangular Scans, 24, 623–633.
568 Loehman, R.E., Rao, C.N.R., and Honig, J.M. (1969) Crystallography and defect chemistry of solid
569 solutions of vanadium and titanium oxides. Journal of Physical Chemistry, 73, 1781–1784.
570 Marcelli, A., Coreno, M., Stredansky, M., Xu, W., Zou, C., Fan, L., Chu, W., Wei, S., Cossaro, A.,

571 Ricci, A., and others (2017) Nanoscale phase separation and lattice complexity in VO2: The
572 metal–insulator transition investigated by xanes via auger electron yield at the vanadium
573 l23-edge and resonant photoemission. Condensed Matter, 2, 1–11.
574 Meunier, J.D. (1994) The Composition and Origin of Vanadium-Rich Clay Minerals in Colorado
575 Plateau Jurassic Sandstones. Clays and Clay Minerals 1994 42:4, 42, 391–401.
576 Mignaioli, E., Capitani, G., Nieto, F., and Mellini, M. (2009) Accurate and precise lattice
577 parameters by selected-area electron diffraction in the transmission electron microscope.
578 American Mineralogist, 94, 793–800.
579 Moretti, R., and Neuville, D.R. (2021) Redox Equilibria, 1–17.
580 Muller, D.A., Fitting Kourkoutis, L., Murfitt, M., Song, J.H., Hwang, H.Y., Silcox, J., Dellby, N., and
581 Krivanek, O.L. (2008) Atomic-scale chemical imaging of composition and bonding by
582 aberration-corrected microscopy. Science, 319, 1073–1076.
583 Mysen, B.O., Virgo, D., and Seifert, F.A. (1984) Redox equilibria of iron in alkaline earth silicate
584 melts: relationships between melt structure, oxygen fugacity, temperature and properties
585 of iron-bearing silicate liquids. American Mineralogist, 69, 834–847.
586 Nicklas, R.W., Puchtel, I.S., and Ash, R.D. (2016) High-precision determination of the oxidation
587 state of komatiite lavas using vanadium liquid-mineral partitioning. Chemical Geology,
588 433, 36–45.
589 Nuñez, M. (2019) Exploring materials band structure space with unsupervised machine
590 learning. Computational Materials Science, 158, 117–123.
591 Ostrooumov, M., and Taran, Y. (2016) Vanadium, V – a new native element mineral from the
592 Colima volcano, State of Colima, Mexico, and implications for fumarole gas composition.

593 Mineralogical Magazine, 80, 371–382.
594 Perdew, J.P., Burke, K., and Ernzerhof, M. (1996) Generalized gradient approximation made
595 simple. Physical Review Letters, 77, 3865–3868.
596 Petit, P.E., Farges, F., Wilke, M., and Solé, V.A. (2001) Determination of the iron oxidation state
597 in Earth materials using XANES pre-edge information. Journal of Synchrotron Radiation, 8,
598 952–954.
599 Prytulak, J., Nielsen, S.G., Ionov, D.A., Halliday, A.N., Harvey, J., Kelley, K.A., Niu, Y.L., Peate,
600 D.W., Shimizu, K., and Sims, K.W.W. (2013) The stable vanadium isotope composition of
601 the mantle and mafic lavas. Earth and Planetary Science Letters, 365, 177–189.
602 Radwany, M. (2021) GEOMETALLURGICAL CHARACTERIZATION OF SANDSTONE-HOSTED
603 VANADIUM ORE FROM THE COLORADO PLATEAU.
604 Radwany, M.R., and Barton, I.F. (2022) The process mineralogy of leaching sandstone-hosted
605 uranium-vanadium ores. Minerals Engineering, 187, 107811.
606 Rakotoniaina, J.C., Mokrani-Tamellin, R., Gavarri, J.R., Vacquier, G., Casalot, A., and Calvarin, G.
607 (1993) The thermochromic vanadium dioxide. I. Role of stresses and substitution on
608 switching properties. Journal of Solid State Chemistry, 103, 81–94.
609 Righter, K., Drake, M.J., and Scott, E.R.D. (2006) Compositional relationships between
610 meteorites and terrestrial planets. Meteorites and the early solar system II, 943, 803–828.
611 Righter, K., Sutton, S.R., Danielson, L., Pando, K., and Newville, M. (2016) Redox variations in
612 the inner solar system with new constraints from vanadium XANES in spinels. American
613 Mineralogist, 101, 1928–1942.
614 Roskosz, M., Dauphas, N., Hu, J., Hu, M.Y., Neuville, D.R., Brown, D., Bi, W., Nie, N.X., Zhao, J.,

615 and Alp, E.E. (2022) Structural, redox and isotopic behaviors of iron in geological silicate
616 glasses: A NRIXS study of Lamb-Mössbauer factors and force constants. Geochimica et
617 Cosmochimica Acta, 321, 184–205.
618 Schreiber, H.D., Thanyasiri, T., Lach, J.J., and Legere, R.A. (1978) REDOX EQUILIBRIA OF Ti, Cr,
619 AND Eu IN SILICATE MELTS: REDUCTION POTENTIALS AND MUTUAL INTERACTIONS. Phys
620 Chem Glasses, 19, 126–139.
621 Simon, S.B., Sutton, S.R., and Grossman, L. (2007) Valence of titanium and vanadium in
622 pyroxene in refractory inclusion interiors and rims. Geochimica et Cosmochimica Acta, 71,
623 3098–3118.
624 Sparrow, T.G., Williams, B.G., Rao, C.N.R., and Thomas, J.M. (1984) L3/L2 white-line intensity
625 ratios in the electron energy-loss spectra of 3d transition-metal oxides. Chemical Physics
626 Letters, 108, 547–550.
627 Stevens, A.J. (2018) Compressive Sensing in Transmission Electron Microscopy. Duke
628 University, 178.
629 Stoyanov, E., Langenhorst, F., and Steinle-Neumann, G. (2007) The effect of valence state and
630 site geometry on Ti L3,2 and O K electron energy-loss spectra of TixOy phases. American
631 Mineralogist, 92, 577–586.
632 Taillon, J.A. (2018) Compressive Sensing Reconstruction for EDS Analysis. Microscopy and
633 microanalysis : the official journal of Microscopy Society of America, Microbeam Analysis
634 Society, Microscopical Society of Canada, 24, 486–487.
635 Tan, H., Turner, S., Yücelen, E., Verbeeck, J., and Van Tendeloo, G. (2011) 2D Atomic Mapping
636 of Oxidation States in Transition Metal Oxides by Scanning Transmission Electron

637 Microscopy and Electron Energy-Loss Spectroscopy.
638 Tan, H., Verbeeck, J., Abakumov, A., and Van Tendeloo, G. (2012) Oxidation state and chemical
639 shift investigation in transition metal oxides by EELS. Ultramicroscopy.
640 Tian, M., Wang, X.D., and Zhang, T. (2016, April 7) Hexaaluminates: A review of the structure,
641 synthesis and catalytic performance. Catalysis Science and Technology. Royal Society of
642 Chemistry.
643 Van Aken, P.A., and Liebscher, B. (2002) Quantification of ferrous/ferric ratios in minerals: New
644 evaluation schemes of Fe L23 electron energy-loss near-edge spectra. Physics and
645 Chemistry of Minerals, 29, 188–200.
646 Van Aken, P.A., Liebscher, B., and Styrsa, V.J. (1998) Quantitative determination of iron
647 oxidation states in minerals using Fe L2,3-edge electron energy-loss near-edge structure
648 spectroscopy. Physics and Chemistry of Minerals, 25, 323–327.
649 Virdi, K.S., Kauffmann, Y., Ziegler, C., Ganter, P., Lotsch, B. V., Kaplan, W.D., Blaha, P., and Scheu,
650 C. (2013) Electronic structure of KCa2Nb3O10 as envisaged by density functional theory
651 and valence electron energy loss spectroscopy. Physical Review B - Condensed Matter and
652 Materials Physics, 87, 115108.
653 Wanty, R.B., and Goldhaber, M.B. (1985) A method for the determination of vanadium and iron
654 oxidation states in naturally occurring oxides and silicates. Talanta, 32, 395–398.
655 Xu, H., and Wang, Y. (1999) Electron energy-loss spectroscopy (EELS) study of oxidation states
656 of Ce and U in pyrochlore and uraninite - Natural analogues for Pu- and U-bearing waste
657 forms. Journal of Nuclear Materials, 265, 117–123.
658 You Zhou, and Ramanathan, S. (2015) Mott Memory and Neuromorphic Devices. Proceedings

659 of the IEEE, 103, 1289–1310.
660 Zanetta, P.-M., Manga, V.R., Chang, Y., Ramprasad, T., Beckett, J.R., Zega, T.J., and Sciences, P.
661 (2022) Atomic-scale characterization of the oxidation state of Ti in meteoritic hibonite:
662 Implications for early solar system thermodynamics. American Mineralogist.
663 Zega, T.J., and Buseck, P.R. (2003) Fine-grained-rim mineralogy of the Cold Bokkeveld CM
664 chondrite. Geochimica et Cosmochimica Acta, 67, 1711–1721.
665 Zega, T.J., Garvie, L.A.J., and Buseck, P.R. (2003) Nanometer-scale measurements of iron
666 oxidation states of cronstedtite from primitive meteorites. American Mineralogist, 88,
667 1169–1172.
668 Zega, T.J., Nittler, L.R., Busemann, H., Hoppe, P., and Stroud, R.M. (2007) Coordinated isotopic
669 and mineralogic analyses of planetary materials enabled by in situ lift-out with a focused
670 ion beam scanning electron microscope. Meteoritics and Planetary Science, 42, 1373–
671 1386.
672 Zega, T.J., Haenecour, P., and Floss, C. (2020) An in situ investigation on the origins and
673 processing of circumstellar oxide and silicate grains in carbonaceous chondrites.
674 Meteoritics and Planetary Science, 55, 1207–1227.
675 Zheng, Q., Zhang, Y., Liu, T., Huang, J., and Xue, N. (2019) Vanadium extraction from black shale:
676 Enhanced leaching due to fluoride addition. Hydrometallurgy, 187, 141–148.
677 Zheng, Q., Zhang, Y., and Xue, N. (2022) Enhancing effect of vanadium releasing efficiently from
678 lattice in black shale by thermal activation. Colloids and Surfaces A: Physicochemical and
679 Engineering Aspects, 651, 129773.
680 Zhou, Y. (2017) Mott Memory and Neuromorphic Devices.

681

682

683

684

685

686

687

688

689

690

Standard	Oxidation state	Space group	Tc for IMT	RMT V a.u.	RMT O a.u.	RKMax ($R_{mt} * K_{max}$)	Energy threshold (Ry)	Final Kmesh points	Initial cif file
V_2O_3	3+	R-3C	160 K	1.84	1.66	7	-6	100	(Newnham and Haan, 2014)
VO_2	4+	$P2_1/c$	340 K	1.61	1.46	7	-6	100	(Rakotoniaina et al., 1993)
V_2O_5	5+	Pmmn	530 K	1.56	1.41	7	-6	100	(Ketelaar, 1936)
Roscoelite (3+)	3+	C2/m	Nd	1.97	1.53	7	-8	100	(Brigatti et al., 2003)
Roscoelite (1:3)	3.75+	C2/m	Nd	1.61	1.46	7	-6	100	(Brigatti et al., 2003)

Table 1: Calculation setup parameters for the SCF calculation of the different species. Space group shown in Hermann-Mauguin notation. IMT: insulator to metal transition. RMT: muffin-tin radius. The sampling points in the Brillouin zone are given as Kmesh. Visualization of the structures is presented in Fig. 1

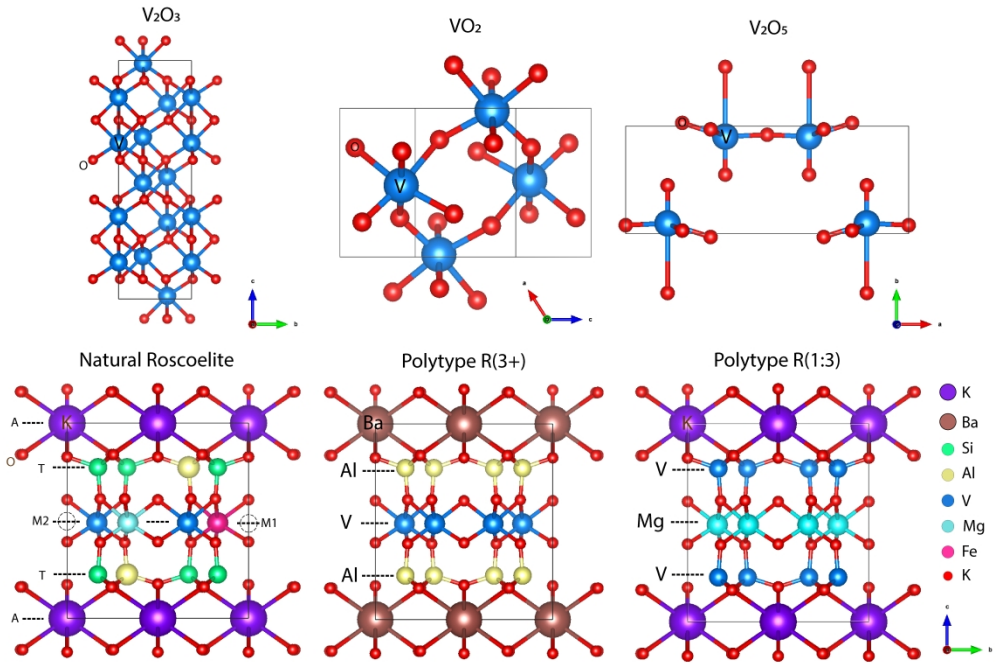

Figure 1 Ball-and-stick representation of the V-compound structures. The structures are presented along the best orientations (a,b or c) to facilitate the visualization of the geometries. Two "idealized" polytypes of the roscoelite crystal are presented R(3+) and R(1:3). They represent a simplified version of the crystal chemistry that respect the space group symmetry. Each color represents one atom. The color code is indicated in the bottom right corner.

593x392mm (300 x 300 DPI)

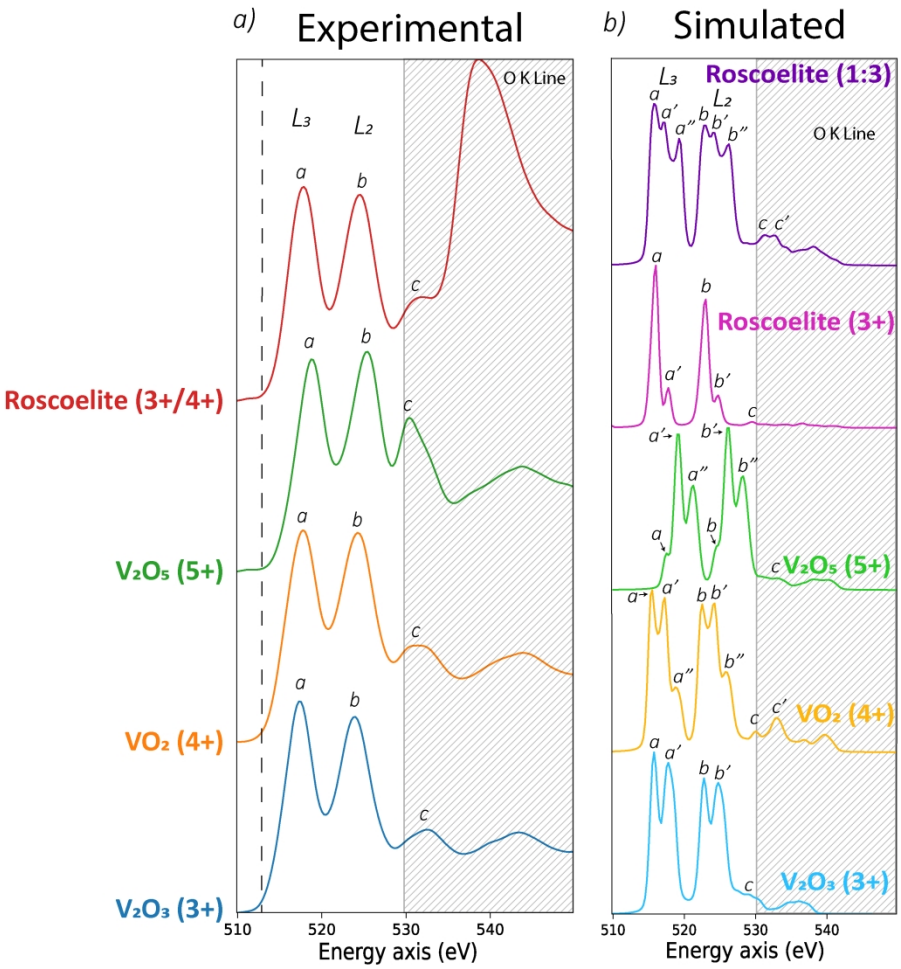

Figure 2: Experimental and simulated VL2,3 spectra normalized to the maximum intensity of the L3 peak. The O K line contribution is not included in the simulation. a) experimental spectra of the V-oxides and the Placerville roscoelite. The O K line is shadowed (gray panel). b) Simulated spectra from Wien2K with limited (0.8 eV) broadening, allowing a more complete description of the spectral features.

290x310mm (300 x 300 DPI)

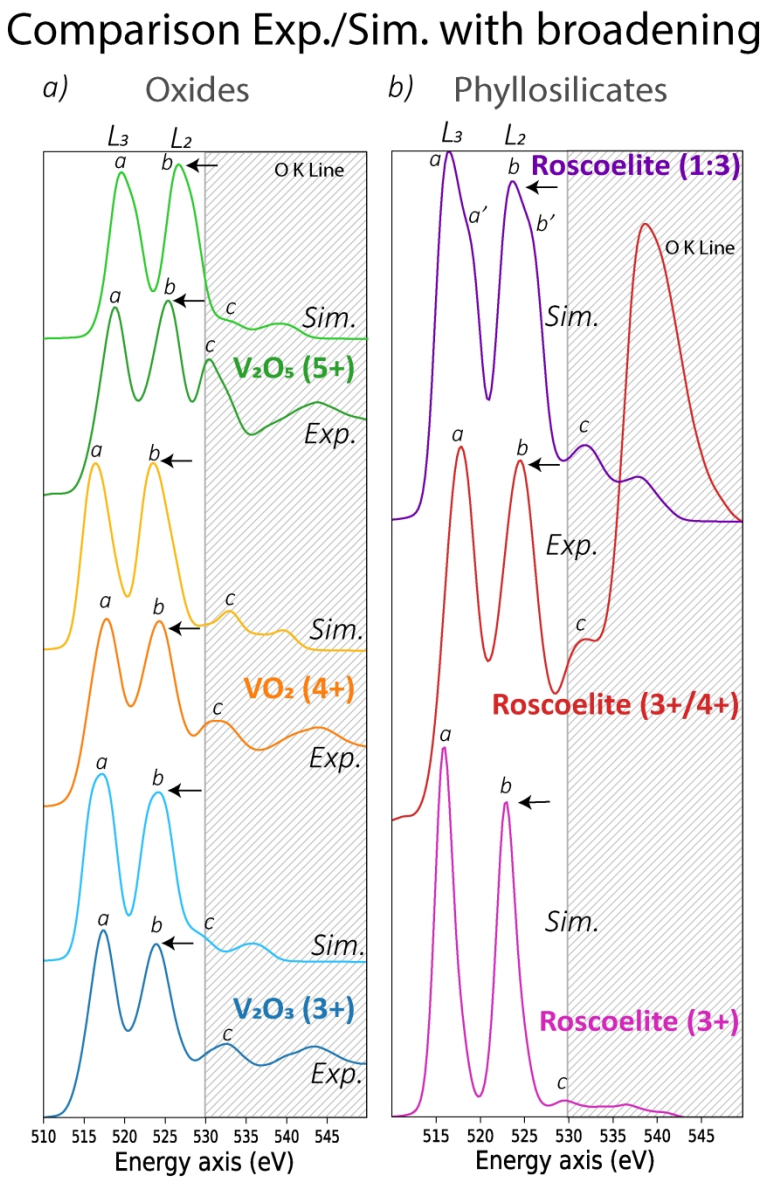

Figure 3: Experimental and simulated VL2,3 spectra normalized to the maximum intensity of the L3 peak. The O K line contribution is not included in the simulation. a) Comparison of the simulated and experimental spectra for the V-oxides only (same color family represent the same structure). The black arrows highlight the increase of the L2 intensity as function of the oxidation state which is reproduced by the simulations. b) Comparison of the experimental and simulated roscoelite materials. The O K line is shadowed.

213x308mm (300 x 300 DPI)

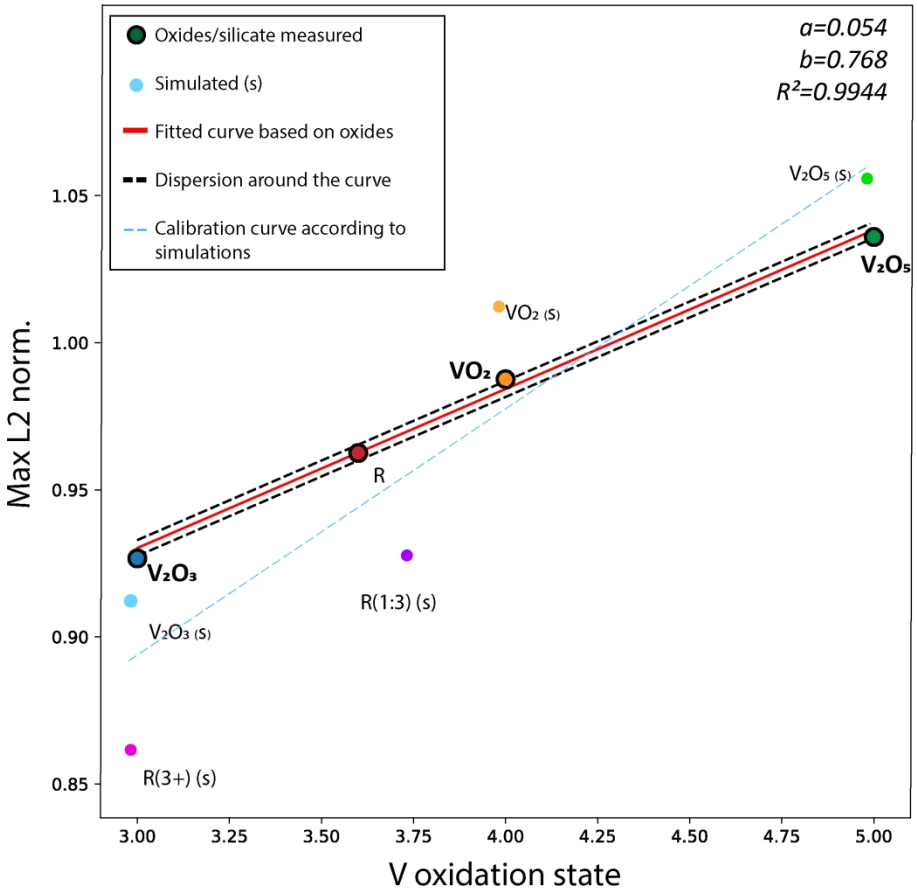

Figure 4: Fitted relationship between the maximum L2 peak height after normalization and the vanadium oxidation state as measured and computed for the oxide standards. Both results from the experimental and simulated spectra are represented. Only the experimental oxide data are used to fit the calibration curve. The theoretical curve fitted based on the simulated spectra is represented (blue dashed line). R=experimental roscoelite. R(3+), R(3:1)= simulated polytypes.

210x201mm (300 x 300 DPI)

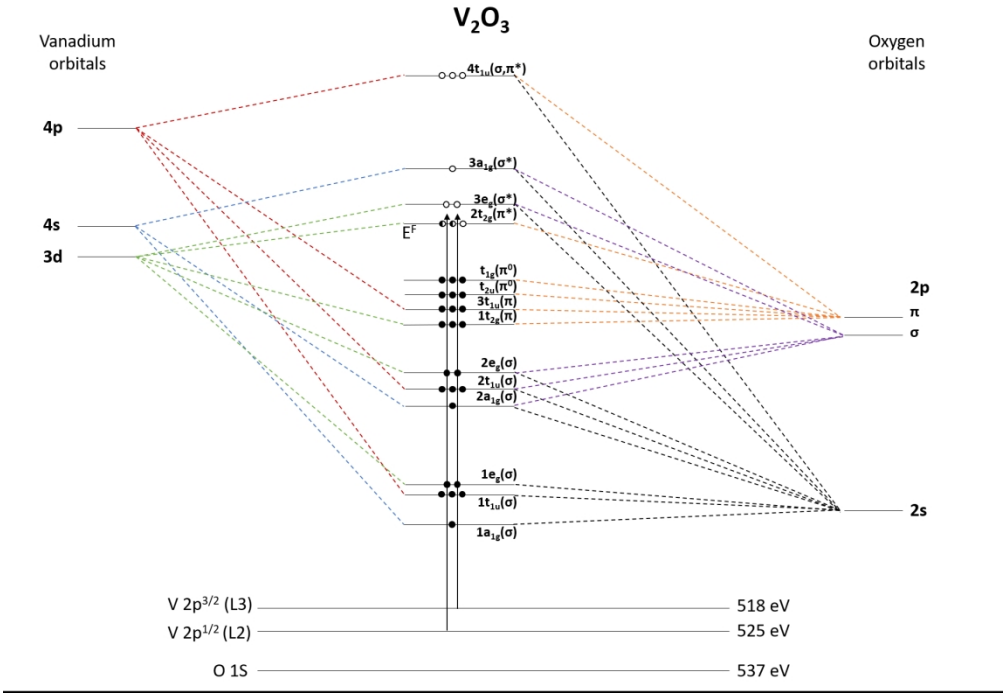

Figure 5: Molecular-orbital diagram for V2O3 with two electrons on the 2t2g level (half-solid circles). Modified after Fischer (1970). The core state leading to the L2 and L3 peak are represented. The transition from the O 1S and the empty state level would correspond to the O K edge (shadowed region of Fig. 2).

339x245mm (150 x 150 DPI)

Table S1. Microprobe measurements of Placerville roscoelite composition, normalized to 7 cations with all V as V_2O_3. Standards, detection limits, and uncertainties are in the Supplementary Information. Other elements (Sn, Co, Ni, Cu, Zr, Y, Sc, As, Ga, F, Cl) were measured but were below detection limits.

Point	Na_2O	MgO	Al_2O_3	SiO_2	K_2O	CaO	V_2O_3	TiO_2	FeO	MnO	UO_2	SrO	P_2O_5	ZnO	PbO	total
1	0.071	0.693	20.475	45.513	9.134	0.232	20.027	0.109	0.763	0.000	0.000	0.039	0.035	0.071	0.000	97.161
2	0.027	0.995	19.912	46.625	9.106	0.257	18.674	0.251	0.997	0.009	0.000	0.032	0.021	0.051	0.000	96.956
3	0.047	0.734	19.285	45.315	9.423	0.235	21.628	0.030	0.724	0.002	0.000	0.030	0.004	0.131	0.000	97.587
4	0.205	0.739	17.612	39.215	7.973	0.803	17.354	10.935	4.838	0.165	0.000	0.045	0.082	0.722	0.202	100.889
5	0.110	0.794	19.223	45.743	9.597	0.189	20.041	0.019	0.993	0.000	1.489	0.023	0.016	0.104	0.006	98.349
6	0.079	0.715	20.293	42.835	10.576	0.191	20.863	0.027	0.941	0.006	0.000	0.034	0.068	0.105	0.014	96.748
7	0.132	0.667	19.140	46.066	9.569	0.170	20.479	0.021	0.806	0.006	0.000	0.022	0.052	0.217	0.000	97.346
8	0.121	0.678	20.199	44.320	9.558	0.201	21.133	0.007	0.813	0.026	0.000	0.031	0.106	0.068	0.000	97.261
9	0.068	0.672	20.151	45.628	9.333	0.158	20.312	0.021	0.750	0.000	0.000	0.027	0.009	0.068	0.000	97.196

SUPPLEMENTARY INFORMATION TABLE – Microprobe standards, detection limits, and uncertainties

element	Na	Mg	Al	Si	K	Ca	V	Ti	Fe	Mn	U	Sr	P	Zn	Pb
σ	0.037	0.041	0.155	0.209	0.182	0.019	0.189	0.024	0.070	0.022	0.004	0.013	0.004	0.013	0.004
det. limit, ppm	365.9	224.3	308.1	265.1	246.4	153.8	228.6	188.6	432.9	385.2	370.0	144.3	38.8	125.0	133.3
name of standard	albite-Cr	ol-fo92	anor-hk	kspar-OR1	kspar-OR1	anor-hk	v_1	rutile 1	fayalite	rhod791	UO2	SrTiO3	ap-synap	ZnO	NBS-K0229

Standard compositions:
albite-Cr = Si : 31.96%, Al : 10.39%, Fe : 0.01%, Ca : 0.01%, Na : 8.77%, K : 0.02%, O : 48.72%
ol-fo92 = Si : 19.13%, Al : 0.02%, Fe : 6.36%, Mn : 0.09%, Mg : 30.33%, Ca : 0.07%, Ni : 0.32%, O : 43.74%
anor-hk = Si : 20.57%, Al : 18.98%, Fe : 0.38%, Mg : 0.05%, Ca : 13.71%, Na : 0.44%, O : 46.08%
kspar-OR1 = Si : 30.10%, Al : 9.83%, Fe : 0.02%, Na : 0.85%, K : 12.39%, Ba : 0.73%, Sr : 0.03%, Rb : 0.03%, H : 0.01%, O : 46.04%
v_1 = V : 100.00%
rutile1 = Ti : 59.93%, O : 40.06%
fayalite = Si : 13.84%, Ti : 0.01%, Al : 0.05%, Fe : 52.24%, Mn : 1.55%, Mg : 0.06%, Ca : 0.21%, Zn : 0.38%, O : 31.45%
rhod791 = Si : 21.66%, Ti : 0.01%, Al : 0.02%, Fe : 2.10%, Mn : 36.14%, Mg : 0.58%, Ca : 2.69%, O : 37.28%
UO2 = U : 88.15%, O : 11.85%
SrTiO3 = Sr : 47.74%, Ti : 26.10%, O : 26.16%
ap-synap = F : 3.77%, P : 18.43%, Ca : 39.74%, O : 38.07%
ZnO = Zn : 80.34%, O : 19.66%
NBS_K0229 = Si : 14.02%, Pb : 64.98%, O : 20.99%

Experimental onset and peak position (eV)

		V203	VO2	V2O5	Roscoelite	
Onset		512.2	512.5	513.2	512.8	
Peak	a	517.4	517.7	518.8	517.8	
	b	523.9	524.2	525.4	524.6	
	c	532.3	531.5	530.4	531.4	
		Simulated onset and peak position (eV)				
		V203	VO2	V2O5	R(3+)	R(1:3)
Onset		512.8	513.2	516.2	513.1	513.6
peak	a	517.0	516.5	59.6	515.9	517.4
	b	524.1	523.5	526.5	522.9	524.5
	c	529.8	532.9	532.9	529.4	531.7

Table S2: Main peak energy position in experimental and simulated (broadened) spectra in eV. The energy given correspond to the center of a fitted Gaussian under the peak.

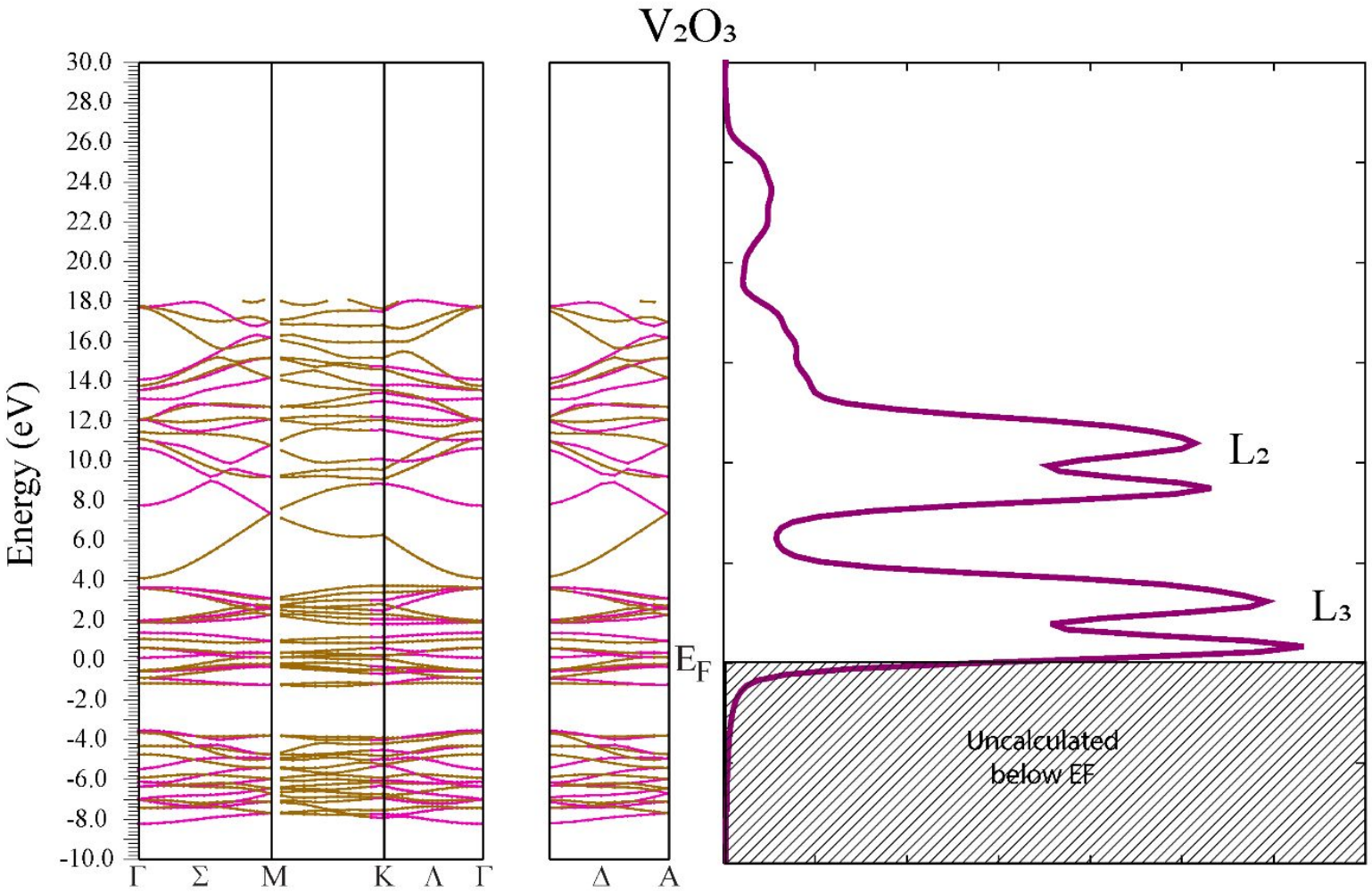

Fig. S1: V_2O_3 band structure and associated simulated (slightly broadened; 0.8 eV) spectra from Wien2K and TELNES 3.